JOURNAL OF AIRCRAFT
Vol. 32, No. 2, March–April 1995

Numerical Simulation of the Jet Produced by an Internal Aircraft Explosion

James A. Mundy,* Donald P. Rizzetta,† and Reid B. Melville‡
Wright Laboratory, Wright-Patterson Air Force Base, Ohio 45433

Steady flowfields about a generic aircraft fuselage were simulated numerically by integration of the Navier-Stokes equations, including a two-equation (k-ε) turbulence model. A steady, sonic, underexpanded jet issuing from a small square aperture in the fuselage surface was used to model the results of an internal explosion that ruptured the aircraft's skin. The computed solutions include simulations of a wind-tunnel test, and of flight at cruise conditions typical of a large transport aircraft. In each case, both the jet-on and jet-off situations were considered. Details of the computations are presented, and features of the flowfield are discussed. Comparisons were made with experimental data in terms of surface static pressure distributions and total pressure loss profiles, and found to be acceptable for engineering purposes.

Nomenclature

C_D = drag coefficient
C_L = lift coefficient
C_p = pressure coefficient, $2[p - (1/\gamma M_\infty^2)]$
C_{ptl} = total pressure loss coefficient, $2[p - (1/\gamma M_\infty^2)] + 1 - \rho(u^2 + v^2 + w^2)$
C_y = coefficient of y component of force
Cm_y = coefficient of moment about y axis, positive tail down
Cm_z = coefficient of moment about z axis, positive tail right, looking downstream
d = aft fuselage diameter, 30.5 cm
k = nondimensional turbulence kinetic energy
M_∞ = freestream Mach number
n = nondimensional distance normal to solid surface
p = nondimensional static pressure
Re = reference Reynolds number, $\rho_\infty u_\infty d/\mu_\infty$
u, v, w = nondimensional Cartesian velocity components in x, y, z directions
x, y, z = nondimensional Cartesian coordinates in streamwise, lateral, and vertical directions
$\bar{y}^+$ = average value of law-of-the-wall coordinate at first mesh point off surface
ε = nondimensional turbulence energy dissipation
θ = circumferential angle, deg
ξ, η, ζ = nondimensional computational coordinates

Subscripts
min = minimum value
s = neglecting jet momentum flux

Introduction

A JET issuing from an aircraft forebody such as would be produced by an internal blast is simulated numerically. The explosive breach of an aircraft fuselage has proven to be disastrous. Not only does the blast cause structural damage, but the aerodynamic forces generated by the resulting flow are powerful and destructive. The stability of the aircraft can be adversely affected, possibly to the point where the aircraft is uncontrollable, and the tremendous aerodynamic forces can easily lead to structural failure of the aircraft. When the fuselage is breached the pressure of the blast and the normal cabin pressure combine to form a strong jet that issues from the hole created by the explosion. The jet momentum flux contributes directly to the loads on the aircraft, and the presence of the jet induces further aerodynamic forces. These forces, which are created by the flow blockage, are caused by a high-pressure region on the fuselage just upstream of the jet, and a low-pressure region just downstream of the jet. The jet wake region also includes complex vortical flow structures. The purpose of this work is to study the aerodynamics of jet expulsion from an aircraft forebody, and thereby predict the aerodynamic loads.

There has been much research done on the jet in crossflow phenomenon, including both experiments and computations. Work has been presented on jets issuing from forebodies,[1–3] and jets of various shapes.[4,5] Previous investigations have pointed out the need for full three-dimensional simulation[6] and good turbulence modeling.[7] The efforts mentioned above were primarily directed at V/STOL thrusted lift,[1,5,6,8] or puncture of high-speed missiles,[2,3] and have therefore dealt either with low-speed flow, $M_\infty < 0.2$, or with a supersonic freestream. While these previous efforts have considered simplified configurations, the current investigation is directed toward a practical simulation of the postblast flowfield about a typical transport aircraft forebody operating at cruise conditions.

The current work makes no attempt to simulate either the rupture phenomenon or the postblast jet decay that would occur in an actual incident. Between these two events there exists a finite time over which the jet expulsion can be considered steady. It is this phase of the blast, which was investigated in a wind-tunnel experiment, that is considered here numerically.

A summary of the equations is given, as is a discussion of the numerical method applied in the simulations. Details of the computations are discussed, along with characteristics of the numerical flowfield. The computed results obtained from the simulation mentioned above are compared to wind-tunnel data[9] taken at $M_\infty = 0.5$, $Re = 10^6$, 0-deg angle of attack, and no yaw angle, with the jet both on and off. Another set of calculations are presented for a typical cruise condition of

---

Received April 29, 1994; presented as Paper 94-1900 at the AIAA 12th Aerodynamics Conference, Colorado Springs, CO, June 20–22, 1994; revision received July 6, 1994; accepted for publication July 6, 1994. This paper is declared a work of the U.S. Government and is not subject to copyright protection in the United States.

*Aerospace Engineer, CFD Research Branch, Aeromechanics Division, WL/FIMC Building 450, 2645 Fifth Street, Suite 7. Member AIAA.

†Research Aerospace Engineer, CFD Research Branch, Aeromechanics Division, WL/FIMC Building 450, 2645 Fifth Street, Suite 7. Associate Fellow AIAA.

‡Aerospace Engineer, CFD Research Branch, Aeromechanics Division, WL/FIMC Building 450, 2645 Fifth Street, Suite 7. Student Member AIAA.

Table 1 Computational mesh parameters

Case	Mesh size	$\Delta\xi_{\min}$	$\Delta\eta_{\min}$	$\Delta\zeta_{\min}$	$\bar{y}^{+}_{\text{jet-off}}$	$\bar{y}^{+}_{\text{jet-on}}$
Wind tunnel	$(103 \times 92 \times 43)$	7.40×10^{-2}	6.88×10^{-2}	7.00×10^{-4}	4.100	3.218
	$(103 \times 92 \times 85)$	7.40×10^{-2}	6.88×10^{-2}	3.50×10^{-4}	1.974	2.029
Cruise	$(103 \times 92 \times 85)$	7.40×10^{-2}	6.88×10^{-2}	9.54×10^{-5}	1.025	1.013

$M_\infty = 0.75$, and $Re = 2.14 \times 10^6$ (30,000 ft, standard day), also at 0-deg angle of attack and no yaw angle, and jet both on and off.

The comparison to experiment provides a means for assessing the validity of numerically simulating an internal fuselage explosion. In addition, resulting surface pressure distributions and aerodynamic force coefficients may be employed by structural and flight controls models in order to determine aircraft vulnerability. Such analyses can then be used to effect modifications that will enhance survivability, as, e.g., by fuselage hardening.

Governing Equations

The governing equations are the unsteady, compressible, three-dimensional, Navier-Stokes equations written in nondimensional, mass-averaged variables and expressed in conservation form. Effects of turbulence were accounted for by specifying a turbulent Prandtl number $Pr_t = 0.90$, and by incorporating a two-equation model for k and ε. The k-ε equations are essentially identical to those developed by Jones and Launder,[10,11] which have been successfully applied to simulate a variety of turbulent flowfields including supersonic slot injection,[12] airfoil static and dynamic stall,[13] and cylinder juncture flows.[14] Sutherland's law for the molecular viscosity coefficient, the perfect gas relationship, and Stokes' hypothesis for the bulk viscosity coefficient were employed to obtain equation closure. A more detailed development of the governing equations is found in Ref. 15.

Numerical Procedure

Solutions to the governing equations were obtained numerically using the implicit approximately factored finite difference algorithm of Beam and Warming.[16] The scheme employed first-order Euler implicit time differencing, and second-order accurate central-difference approximations for all spatial derivatives. Common forms of both implicit and explicit nonlinear dissipation[17] were utilized to augment stability. In the jet-on cases, the nonlinear dissipation was spatially scaled in the immediate vicinity of the jet opening. This stabilized the solution in areas of high pressure and velocity gradients surrounding the jet, without degrading the solution in regions of smooth flow. Subiterations[18,19] were also used to enhance stability in the jet-on cases, thus allowing a larger time step.

The flow was assumed to be fully turbulent, and no attempt was made to predict the location of transition. This approximated the wind-tunnel test,[9] where a boundary-layer trip tape was installed 0.417d downstream of the nose of the model.

Computational Mesh

A Cartesian coordinate system is oriented as shown in Fig. 1, with the origin at the nose of the fuselage. The forebody transitions to a cylinder of diameter d behind the jet area, and the overall length of the fuselage was 10d. For this study, the jet was modeled as a square hole with edge length of $d/6$. The jet centerline was $5d/2$ from the fuselage nose and was located at $\theta = 135$ deg. The leading and trailing edges of the jet were located at $x = 2.417$ and 2.583, respectively.

Two basic grid sizes were used: 1) a coarse grid of $103 \times 92 \times 43$ points in the axial, circumferential, and normal directions, and 2) a finer grid of $103 \times 92 \times 85$ points. A C-O topological structure in the streamwise and circumferential directions was employed, and the coordinate directions used in both the wind tunnel and cruise simulations were ξ running fore-to-aft along the fuselage, starting at the nose, η wrapping circumferentially starting at the top center of the fuselage, and ζ extending out from the fuselage in a normal direction to the outer boundary of the computational domain.

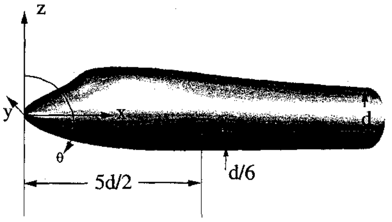

Fig. 1 Fuselage geometry.

All grids were generated with an elliptical grid generation software package,[20] clustering grid points around the jet opening, and at the surface of the fuselage in an effort to gain the best possible resolution for both the jet and the boundary layer. The mesh parameters are listed in Table 1. Complete details of grid construction and the boundary conditions are given in Ref. 15.

Details of the Computations

Initial conditions were formulated on a coarse grid and the flowfields were marched in time toward the steady state employing the previously described numerical algorithm. After convergence was achieved, the coarse-grid solutions were interpolated onto the fine computational mesh. Convergence was determined by monitoring the change in skin friction and surface pressure on the fuselage. Solutions were considered converged when these values exhibited no appreciable change (less than 1%) over 1000 iterations. Calculation of the jet-off cases employed local time stepping, with a Courant-Friedrichs-Lewy (CFL) number of 2.5. The jet-on case proceeded in a time-accurate mode with a nondimensional time step of 0.001 and a single subiteration with a nondimensional time step of 0.0001. All solutions were generated employing the diagonalized form[21] of the numerical algorithm in order to minimize the use of computational resources. Approximately 5000 iterations were required once the solution was interpolated to the fine grid to bring the solution to convergence for the jet-off situation. The jet-on solution exhibits local unsteadiness in the vicinity of the jet, and was time-averaged over 5000 iterations once the steady portion of the flowfield had converged. This time interval corresponds approximately to one period of the fundamental frequency of the unsteadiness.

Results

Details of the Flow

The flowfield generated in the jet-off cases for both the cruise and wind-tunnel simulations was relatively simple. The flow stagnated at the nose of the fuselage, and another high-pressure region formed just upstream of the cockpit. The surface static pressure dropped as the flow accelerated around the bulge in the fuselage, and then recovered as the fuselage thinned. The surface static pressure field for the jet-off case of the wind-tunnel simulation is illustrated in the top of Fig. 2, which also indicates the streamwise x locations where experimental measurements were taken.

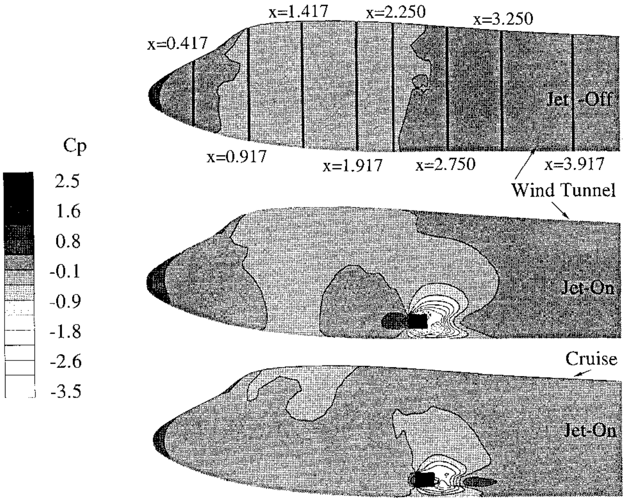

Fig. 2 Static surface pressure contours.

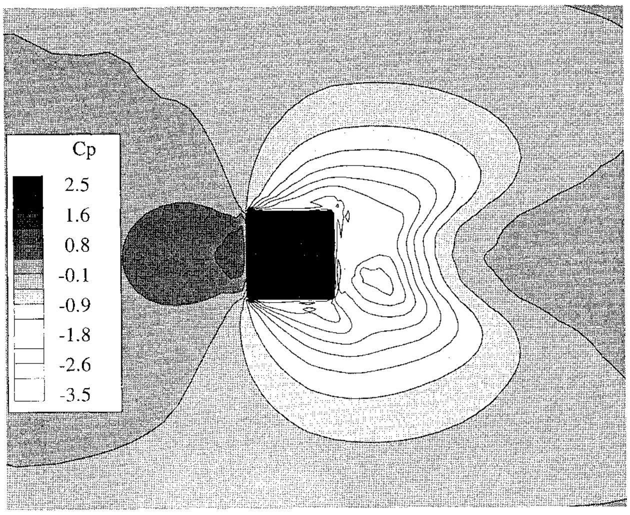

Fig. 3 Static surface pressure contours near jet opening for wind-tunnel simulation.

The middle portion of Fig. 2 is surface static pressure contours for the jet-on case of the wind-tunnel simulation. The pressure distribution indicates a rather complex flowfield. As in the jet-off case, there are high-pressure regions at the nose and just upstream of the cockpit, and the pressure drops as the flow accelerates around the bulge in the fuselage. The flow blockage caused by the jet changes the picture rather dramatically, however. A high-pressure region forms just upstream of the aperture due to stagnation of the oncoming flow. Three distinct vortical structures can be identified on either side of the jet centerline. A horseshoe vortex forms about the jet and is convected downstream around the opening. A pair of counter-rotating primary vortices form behind the jet trailing edge and follow the jet plume. These in turn give rise to secondary vortices that lie between the primaries and close to the fuselage surface. Each secondary vortex rotates in a direction opposite its generating primary. Downstream of the primary vortices is another region of high pressure whose center is approximately 3.5 jet widths aft of the orifice trailing edge. This high-pressure region is associated with a deceleration of the flow that occurs at a node of attachment in the limiting surface streamline pattern.

The bottom of Fig. 2 shows the same flow features mentioned above for the cruise simulation. Even with the higher freestream Mach number of the cruise conditions, the flow remains subcritical except within the jet plume.

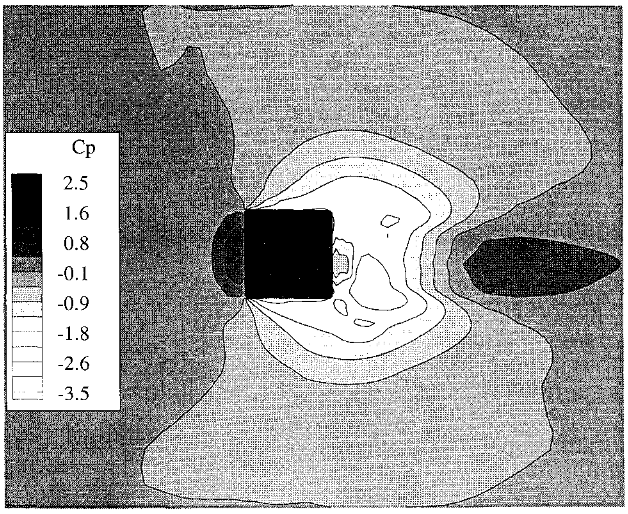

Fig. 4 Static surface pressure contours near jet opening for cruise simulation.

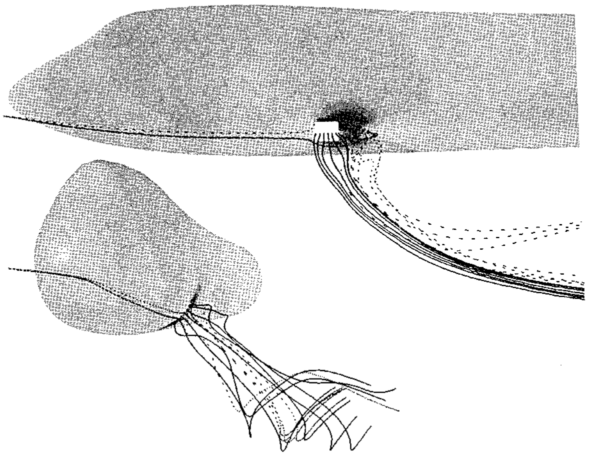

Fig. 5 Particle paths for cruise simulation.

Figure 3 is a close-up of the wind-tunnel simulation jet region, depicting surface static pressure contours in that region. Flow is from left-to-right. The high-pressure regions immediately upstream of the jet and downstream of the primary vortices are seen, as are the low-pressure regions to the side and rear of the jet, which indicate the presence of vortices to the sides of the jet and the primary vortices aft of the jet.

Figure 4 is a similar view for the cruise simulation jet-on case. It is seen that the stagnation regions upstream and downstream of the jet are somewhat stronger than in the wind-tunnel simulation. In addition, the upstream stagnation region lies closer to the jet leading edge. Both of these effects are attributed to the higher freestream Mach number. The stagnation region downstream of the jet is stronger in the cruise simulation because the higher streamwise velocity confines the flow around the jet to a narrower band, and does not allow the secondary vortices to bend around the fuselage as quickly as in the wind-tunnel simulation. Note that the low-pressure region about the jet in Figs. 3 and 4 is smaller in the cruise simulation due to the confining effect of the higher freestream Mach number mentioned above.

Features of the flow structure for the cruise simulation are presented in Figs. 5–9. These same features were seen in the wind-tunnel case. Figure 5 indicates the trajectory of particle paths. The solid traces are for particles released from the jet, while the dashed ones are for particles released upstream and entrained into the primary vortices from the oncoming flow. Particles released at identical locations in the jet opening in

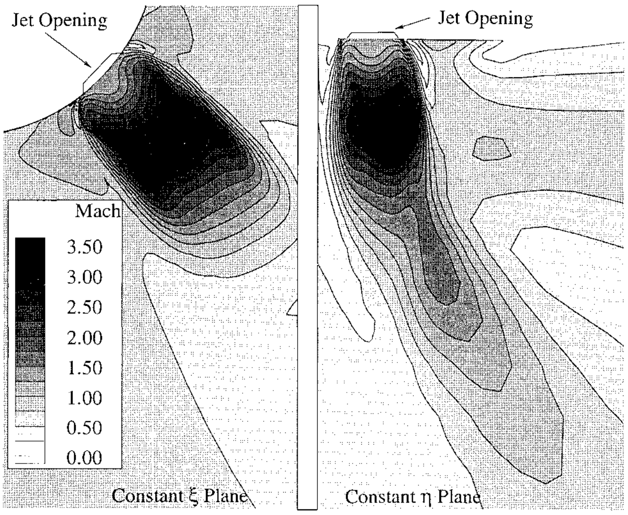

Fig. 6 Mach number contours for cruise simulation at a constant-η plane and constant-ξ plane through jet center.

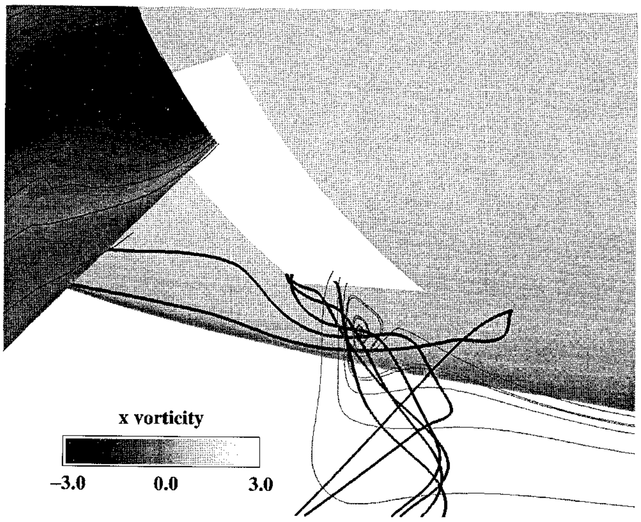

Fig. 8 Particle paths and contours of streamwise component of vorticity for cruise simulation.

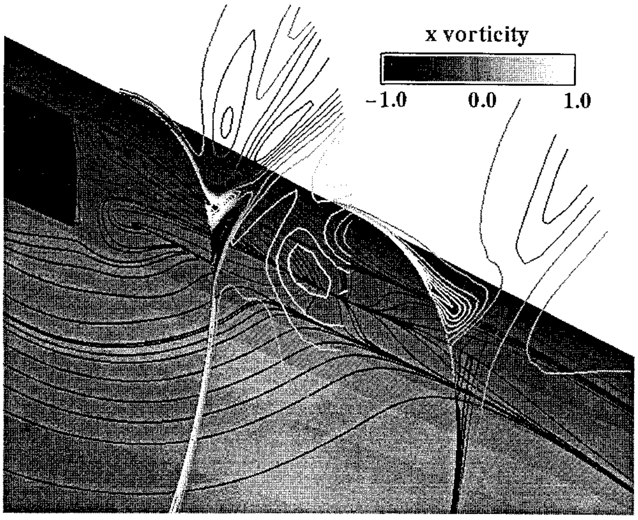

Fig. 7 Surface limiting streamline patterns and contours of streamwise component of vorticity for cruise simulation.

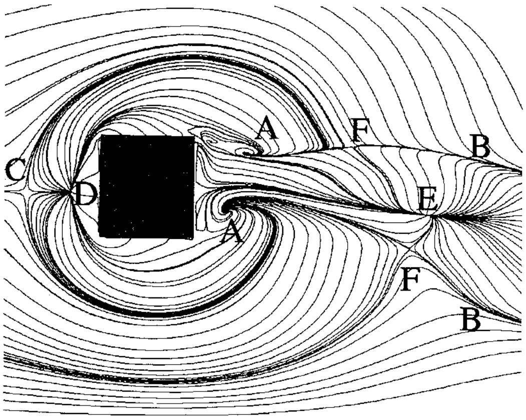

Fig. 9 Limiting surface streamline patterns for cruise simulation.

the wind-tunnel simulation indicate that the jet plume follows the same trajectory for both wind-tunnel and cruise cases. The plume bends sharply to align with the freestream flow. Initially, the jet expands dramatically upon exiting the fuselage, as the divergence of the solid particle traces in Fig. 5 indicates. The Mach number contours in the constant-η plane in Fig. 6 show that the jet expands to approximately 1.5 times the size of the jet opening in the streamwise direction. The Mach number contours for the plane of constant ξ in Fig. 6 show the plume expanding to approximately 2.0 times the size of the opening in the cross stream direction. Note that the flow in the jet plume is supersonic, reaching Mach 3;.5. A barrel-shaped shock around the edges of the jet plume is apparent in both sides of Fig. 6. The top of the shock is somewhat smeared due to lack of grid resolution in that region.

Two primary vortices formed by fluid in the upstream boundary layer follow the jet plume as indicated by the dashed particle traces in Fig. 5. Due to viscous dissipation and grid coarseness, the vortices become indistinguishable from each other as they are convected downstream. Surface limiting streamlines and x component of vorticity contours for the cruise simulation are presented in Fig. 7. The footprint of the primary vortices appears as two spiral foci just downstream of the jet opening. The two secondary vortices indicated in Fig. 7 are induced by and rotate counter to the primary vortices. They appear in the figure as regions with vorticity of opposite sign, and are delineated by the lines of coalescence on the fuselage. Unlike the primaries, the secondary vortices remain in close proximity to the body surface as they are convected downstream. The horseshoe vortex contributes to the low-pressure regions on either side of the jet as seen in Figs. 3 and 4. Streamwise component of vorticity contours and particle paths are displayed in Fig. 8. The thinner particle traces are restricted to a cross plane to better show the formation of the vortex, while the thicker particle traces indicate the vortex is formed by fluid issuing from the corner of the jet and by fluid entrained from the upstream boundary layer. The spiral motion typically associated with such vortices[2,3] is not evident ahead of the orifice, but does appear further downstream. The horseshoe vortex continues downstream next to the jet opening before being wrapped up into the primary vortices.

Limiting surface streamline patterns in the region surrounding the jet opening are shown in Fig. 9. The footprint of the primary vortices can be seen as the two spiral foci, A, just downstream of the jet opening. Two lines of coalescence, B, that trail downstream from the two spiral foci demonstrate the presence of the secondary vortices. Other topological features seen in Fig. 9 are C, a saddle of attachment; D, a node of attachment; E, a node of attachment; and F, saddles of separation. Note that near the surface, although the flow is not symmetric, all topological features appear on both sides of the jet centerline, in approximately the same locations.

Table 2 Force coefficients

Case	C_D	C_L	C_y	C_{Ls}	C_{ys}	Cm_y	Cm_z
Coarse grid wind-tunnel jet-off	5.768	−0.005	0.006	——	——	−0.140	−0.003
Fine grid wind-tunnel jet-off	5.683	0.017	−0.010	——	——	−0.162	0.008
Fine grid cruise jet-off	2.614	0.054	0.040	——	——	−0.177	−0.131
Coarse grid wind-tunnel jet-on	5.673	0.598	0.694	−0.194	−0.060	−1.343	−0.840
Fine grid wind-tunnel jet-on	5.750	0.718	0.800	0.100	−0.016	−1.882	−1.936
Fine grid cruise jet-on	2.664	0.362	0.340	0.038	−0.015	−0.890	−0.685

Force and Moment Coefficients

The force coefficients C_L, C_D, and C_y were calculated from an integration of pressure and shear stresses over the model surface. The contribution of momentum flux from the jet was included in the integration in the jet-on cases. Table 2 lists the coefficients for the jet-off and jet-on cases for both the wind-tunnel and cruise simulations. No force or moment data was taken during the wind-tunnel testing. Given the configuration of the model, essentially a blunt cylinder symmetric about the $y = 0$ plane, one would expect C_D to be the largest of the coefficients, with C_L small and $C_y = 0$ for the jet-off cases. The nonzero values of C_y are, therefore, an indication of the numerical accuracy as influenced by the asymmetric computational mesh. The large value of the force coefficients, particularly C_D, is due in part to the reference area used in the calculations (aft fuselage cross-sectional area, $\pi d^2/4$), which is small compared to the more typical reference of wetted surface area (approximately $10\pi d^2$).

Recall, in comparing the cruise and wind-tunnel results, that the cruise cases were calculated at a Reynolds number approximately twice that of the wind-tunnel cases. The higher Reynolds number used in the cruise simulation accounts for the much lower values of C_D seen in the cruise cases, since the stress terms are proportional to $1/Re$.

In the jet-on cases, the lift and side force coefficients were significantly larger than in the jet-off cases, as expected. The jet did not change the drag coefficient by any large amount. Interestingly, if the contribution of the momentum flux from the jet is neglected, the lift and side force coefficients C_{Ls} and C_{ys} are very small, indicating that the changes in the pressure distribution on the fuselage due to the jet do not add to the overall forces on the fuselage. Referring to Figs. 3 and 4, the high-pressure regions upstream of the jet, in the jet, and downstream of the jet are effectively balanced by the low-pressure region to the sides and rear of the jet opening. These regions of high and low pressure integrate over area into forces acting normal to the fuselage, but in opposite directions. When the momentum flux is included, however, significant side and lifting forces occur.

Examining the pitch and yaw moment coefficients Cm_y and Cm_z, it is apparent that the jet causes the tail of the fuselage to pitch up and to yaw to the left, as one looks downstream. Recall that the origin is located at the nose of the fuselage. The jet-off cases for both the cruise and wind-tunnel simulations show very small moment coefficients. As was true of the side force coefficient C_y, the small nonzero values of Cm_z for jet-off cases indicate the influence of the asymmetric computational mesh on the accuracy of the solutions.

Comparing the coefficients from the fine grid results to the results from the coarse grid computations, there is obvious grid dependence in the solutions. The comparison of experimental results to computational results indicates that the fine grid provided a solution with reasonable engineering accuracy. A more thorough grid resolution study is required to determine the resolution necessary for grid independence.

Comparison to Experiment

As previously noted, the flowfield generated by the clean fuselage was simple, like that generated by a blunt-nosed cylinder. Pressure was generally constant around a circumferential ring, as shown in Figs. 10 and 11, which are surface static pressure distributions for stations upstream and downstream of the jet opening, respectively. Recall that the labeled lines in Fig. 2 refer to the stations at which the data in Figs. 10 and 11 were taken. Figure 10 shows at $x = 0.417$, a distinct rise in pressure near the top of the model due to the shape of the fuselage. Pressures at $x = 0.917$ also exhibit some differences with θ, due to the influence of the cockpit at that station. The correspondence between the numerical results and wind-tunnel data is generally good.

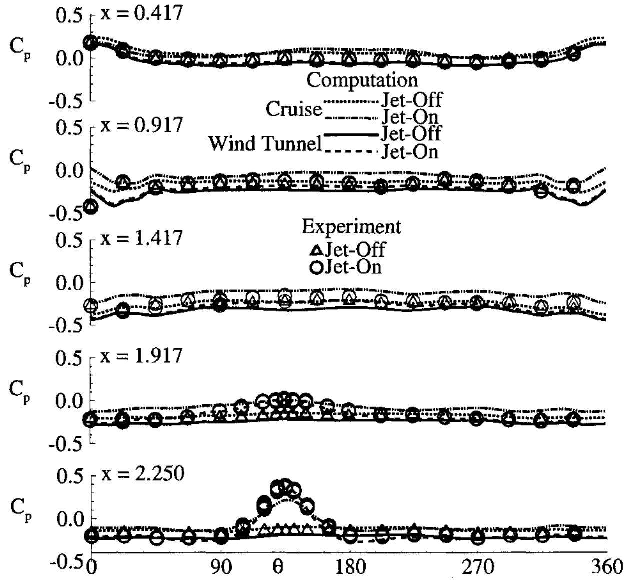

Fig. 10 Static surface pressure distributions at stations upstream of the jet.

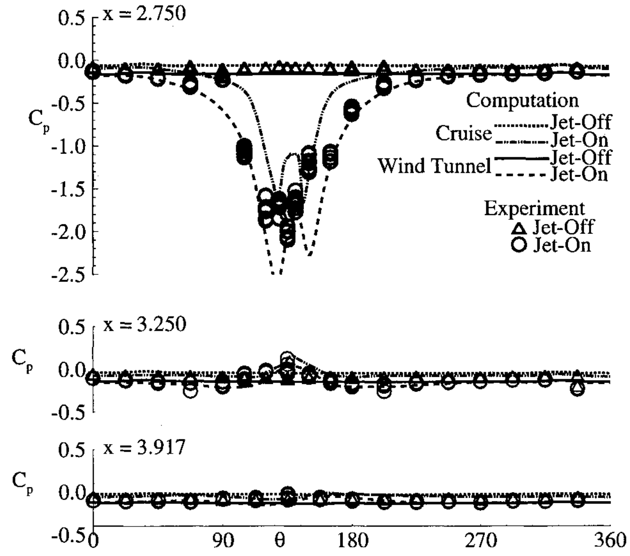

Fig. 11 Static surface pressure distributions at stations downstream of the jet.

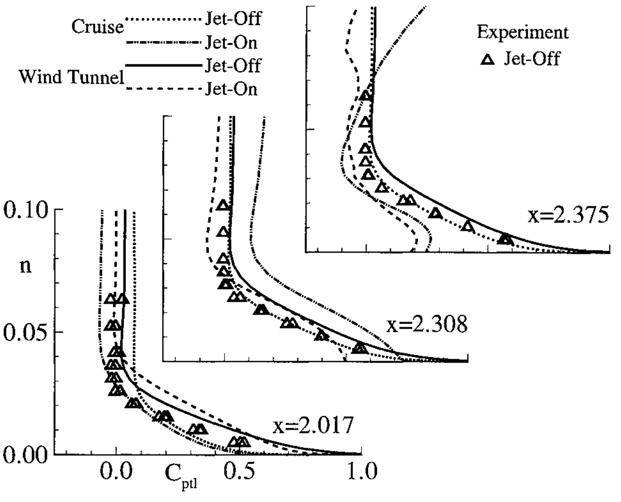

Fig. 12 Total pressure loss profiles upstream of the jet.

Examining Figs. 10 and 11, the effects of the jet on pressure are obvious. The jet causes a pressure rise upstream of the jet opening ($x = 2.250$) due to stagnation of the incoming flow, and a pressure drop downstream of the jet ($x = 2.750$) because of expansion and the formation of vortices. At $x = 3.250$, the small area of high pressure downstream of the low-pressure region behind the jet opening is evident, as was noted in Figs. 2–4. The slight ripple appearing in Fig. 11 for $x = 3.917$ at $\theta = 135$ deg indicates the presence of the secondary vortices seen in Figs. 7 and 9.

Boundary-layer data, in the form of total pressure loss coefficient, is displayed in Fig. 12 for the three stations at which data were gathered in the wind-tunnel test, $x = 2.017$, 2.308, 2.375. Data at all three x locations was taken at 5 and 10 deg on either side of the jet centerline, and on the jet centerline at the $x = 2.017$ station. Recall that the jet leading edge is located at $x = 2.417$. There was little variation displayed with respect to θ. Figure 12 shows classic boundary-layer profiles, with the boundary-layer growing in thickness with increasing x. Figure 12 also shows that the jet caused the boundary layer to become thicker, which is expected since the jet causes a large adverse pressure gradient upstream of the jet exit. Agreement between experimental data and computational results is acceptable, though the computational results tend to overpredict the boundary-layer thickness.

The plot at $x = 2.375$ displays a boundary-layer disrupted by the jet. Referring to Figs. 2–4 note that this x location falls within the stagnation region just upstream of the jet. Flow separation upstream of the station, indicated in Fig. 9, and flow entrainment by the jet combine to give the profile seen in Fig. 12 at $x = 2.375$.

A total pressure rake was used to capture the jet plume profile. The plume rake was installed perpendicular to the fuselage at the jet centerline ($\theta = 135$ deg) in two locations downstream of the jet opening, $x = 2.767$ and 2.958. A comparison of numerical total pressure loss to experimental plume rake results is shown in Fig. 13. Both experimental and numerical values exhibit first a rise, and then a large drop in total pressure loss before recovering to freestream levels. These peaks indicate the presence of the primary vortices (the increase), and then the jet plume (the decrease). The agreement displayed is reasonable given the coarseness of the grid and the unsteady nature of the flow in the region considered. Another factor that contributes to the variation of computational results from experimental data is the fact that the plume rake installed on the model exhibited considerable vibration both from side-to-side and from front-to-back during the tests. Figure 14 shows the circumferential variations in total pressure loss coefficient, with comparison to the experimental data, at the $x = 2.767$ plume rake station. There is significant variation in the jet plume with change in θ. The variation was greater with reduction in θ (toward the top of the fuselage), than with increasing θ. This trend is not surprising, since the trajectory of the jet plume and its associated vortices tended to shift toward the underside of the fuselage, as seen in Figs. 5 and 7. In other words, reducing θ moves away from the direction of the jet plume's path, whereas increasing θ moves in the direction of the jet plume's trajectory.

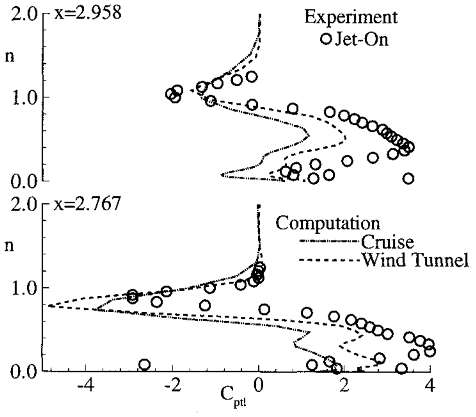

Fig. 13 Total pressure loss profiles downstream of the jet.

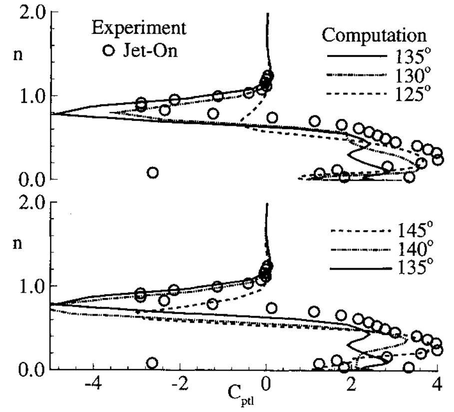

Fig. 14 Circumferential variation of total pressure loss profiles at $x = 2.767$ for wind-tunnel simulation.

Concluding Remarks

Four cases were considered in this study, jet-on and jet-off cases for the simulation of both a wind-tunnel test and cruise conditions typical for a large transport aircraft. Results of the numerical simulation were compared to data from the wind-tunnel test in the form of surface static pressure coefficient, and total pressure loss coefficient profiles. Agreement was generally acceptable, even in the region just downstream of the jet.

The jet caused strong side and lifting forces, which in a real aircraft would result in yaw and pitch. The pressure field on the fuselage surface was dramatically changed locally by the presence of the jet, but in terms of total force contribution, the change was minimal. The force contribution of the mass flow from the jet, however, was significant. In spite of the fact that the pressures over the entire fuselage cancel out in integration, the pressure field indicates potentially large forces acting normal to the surface, but in opposing directions. The possibility of structural damage given such a load is high.

In conclusion, the computations indicate that a strong jet in a high subsonic crossflow can be successfully modeled for practical applications. The resulting flowfield is complex, with numerous vortices, strong pressure gradients, and a shock structure around the jet. Knowing the structure of the flowfield is the first step in making the rupture of an aircraft fuselage a more survivable event.

Acknowledgments

The work presented here was supported by the Federal Aviation Administration, under research agreement FAAF9101. Computational resources for this work were provided through the auspices of the Air Force Super Computer Center, Kirtland AFB, New Mexico, and the DoD High Performance Computing Center at the U.S. Army Corps of Engineers Waterways Experiment Station, Vicksburg, Mississippi. The authors are grateful to a number of individuals at Wright Laboratory, Wright-Patterson AFB, Ohio, without whose assistance this effort would not be possible. These include Gregory O. Stecklein for management of administrative details, Dennis L. Carter, Rodney L. Clark, and Gary A. Dale for help in analyzing the experimental data, John Shaner for assistance in extracting the data from computer records, and Miguel R. Visbal for helpful discussions.

References

[1] Schetz, J. A., Jakubowski, A. K., and Aoyagi, K., "Jet Trajectories and Surface Pressures Induced on a Body of Revolution with Various Dual Jet Configurations," *Journal of Aircraft*, Vol. 20, No. 11, 1983, pp. 975–982.

[2] Shang, J. S., McMaster, D. L., and Buck, M., "Interaction of Jet in Hypersonic Cross Stream," *AIAA Journal*, Vol. 27, No. 3, 1989, pp. 323–329.

[3] McMaster, D. L., Shang, J. S., and Golbitz, W. C., "Supersonic, Transverse Jet from a Rotating Ogive Cylinder in a Hypersonic Flow," *Journal of Spacecraft and Rockets*, Vol. 26, Jan.–Feb. 1989, pp. 24–30.

[4] Krothapalli, A., Lourenco, L., and Buchlin, J., "On the Separated Flow Upstream of a Jet in Cross Flow," AIAA Paper 89-0571, Jan. 1989.

[5] Kavsaoglu, M. S., Schets, J. A., and Jakubowski, A. K., "Rectangular Jets in a Crossflow," *Journal of Aircraft*, Vol. 26, No. 9, 1989, pp. 793–804.

[6] Roth, K. R., "Influence of the Thin-Layer Approximation on Jet in Crossflow Computations," AIAA Paper 90-3056, Aug. 1990.

[7] Lytle, J. K., Harloof, G. J., and Hsu, A. T., "Three-Dimensional Compressible Jet-in-Crossflow Calculations Using Improved Viscosity Models and Adapted Grid," AIAA Paper 90-2100, July 1990.

[8] Oh, T. S., and Schetz, J. A., "Finite Element Simulation of Jets in a Crossflow with Complex Nozzle Configurations for V/STOL Applications," AIAA Paper 88-3269, July 1988.

[9] Carter, D. L., Clark, R. L., Dale, G., and Stecklein, G. O., "Aircraft Hardening Program, Aeromechanics Experimental Data Report," WL-TR-94-3029, Wright-Patterson AFB, OH, March 1994.

[10] Jones, W. P., and Launder, B. E., "The Prediction of Laminarization with a Two-Equation Model of Turbulence," *International Journal of Heat and Mass Transfer*, Vol. 15, Feb. 1972, pp. 301–314.

[11] Jones, W. P., and Launder, B. E., "The Calculation of Low-Reynolds-Number Phenomena with a Two-Equation Model of Turbulence," *International Journal of Heat and Mass Transfer*, Vol. 16, June 1973, pp. 1119–1130.

[12] Rizzetta, D. P., "Numerical Simulation of Slot Injection into a Turbulent Supersonic Stream," *AIAA Journal*, Vol. 30, No. 10, 1992, pp. 2434–2439.

[13] Rizzetta, D. P., and Visbal, M. R., "Comparative Numerical Study of Two Turbulence Models for Airfoil Static and Dynamic Stall," *AIAA Journal*, Vol. 31, No. 4, 1993, pp. 784–786.

[14] Rizzetta, D. P., "Numerical Simulation of Turbulent Cylinder Juncture Flowfields," *AIAA Journal*, Vol. 32, No. 6, 1994, pp. 1113–1119.

[15] Mundy, J. A., Rizzetta, D. P., and Melville, R. B., "Numerical Simulation of Jet Expulsion from an Aircraft Fuselage," AIAA Paper 94-1900, June 1994.

[16] Beam, R., and Warming, R., "An Implicit Factored Scheme for the Compressible Navier-Stokes Equations," *AIAA Journal*, Vol. 16, No. 4, 1978, pp. 393–402.

[17] Jameson, A., Schmidt, W., and Turkel, E., "Numerical Solutions of the Euler Equations by Finite Volume Methods Using Runge-Kutta Time Stepping Schemes," AIAA Paper 81-1259, June 1981.

[18] Rizzetta, D. P., and Visbal, M. R., "Comparative Numerical Study of Two Turbulence Models for Airfoil Static and Dynamic Stall," *AIAA Journal*, Vol. 31, No. 4, 1993, pp. 784–786.

[19] Gordnier, R. E., and Visbal, M. R., "Numerical Simulation of the Unsteady Vortex Structure over a Delta Wing," AIAA Paper 91-1811, June 1991.

[20] Steinbrenner, J. P., Chawner, J. P., and Fouts, C. L., "The GRIDGEN 3D Multiple Block Grid Generation System, Volume II: User's Manual," WRDC-TR-90-3022, Wright Research and Development Center, Feb. 1991.

[21] Pulliam, T. H., and Chaussee, D. S., "A Diagonal Form of the Implicit Approximate-Factorization Algorithm," *Journal of Computational Physics*, Vol. 39, Feb. 1981, pp. 347–363.